Available online at www.sciencedirect.com
ScienceDirect
Trans. Nonferrous Met. Soc. China 34(2024) 3876−3892
Transactions of Nonferrous Metals Society of China
www.tnmsc.cn

Microstructure and mechanical properties of directly thixoforged complex box-shape 2A14 part with large wall-thickness difference

Ying-ze LIU[1], Ju-fu JIANG[1], Ying ZHANG[1], Min-jie HUANG[1], Jian DONG[1], Ying WANG[2]

1. National Key Laboratory for Precision Hot Processing of Metals, School of Materials Science and Engineering, Harbin Institute of Technology, Harbin 150001, China;
2. School of Mechatronics Engineering, Harbin Institute of Technology, Harbin 150001, China

Received 14 April 2023; accepted 5 September 2023

Abstract: To form complex box-shape parts with large wall-thickness difference, a directly thixoforged technology of 2A14 alloy with low-cost and short-process was proposed and verified. The results showed that complex components were successfully thixoforged. Solid grains in the microstructure of the thixoforged parts exhibited a large deformation degree. This led to an obvious improvement in the mechanical properties of the thixoforged parts. No obvious liquid segregation was found in the microstructure. High mechanical properties were obtained in the thixoforged 2A14 alloy components. The yield strength varied from 157.1 to 187.3 MPa, the ultimate tensile strength varied from 268.2 to 316.6 MPa, and the elongation varied from 7.8% to 24.9%. Increase in plastic deformation degree caused by larger size and less round grains is beneficial to the mechanical properties of the thixoforged components.
Key words: thixoforging; microstructure; mechanical properties; 2A14 aluminum alloy

1 Introduction

2A14 aluminum alloy, also known as 2014 aluminum alloy, has the characteristics of high strength and light weight [1,2]. As the second most popular 2000 series deformed aluminum alloy with the amount of 2024 aluminum alloy, it has better thermal strength than 2024 aluminum alloy, so it is often used in aircraft heavy forging, thick plates, wheels, rocket fuel tanks and other parts requiring certain thermal strength [3−5]. Due to the wide temperature range of the semi-solid, there is obvious hot cracking behavior in solidification forming, which is difficult to form by casting [6]. Semisolid processing technology is a method for achieving near-net-shape forming of complex structures. Since its proposal, semisolid processing technology has been successfully applied in a large number of engineering projects, particularly in the forming of various cast aluminum alloys [7,8] and cast magnesium alloys [9−12]. The extent to which semisolid processing technology has replaced gravity casting technology in enhancing the mechanical properties of formed parts has been a remarkable success [13].

However, the application of semisolid processing technology in deformed aluminum alloys is mostly in the laboratory stage, and there are still many problems to be solved before the large-scale engineering application [14]. Many scholars have explored various billet-making methods for aluminum alloys. MESHKABADI et al [15] used equal channel angular extrusion (ECAP) deformation and semisolid isothermal treatment (SSIT) process to prepare the semi-solid billet of 7075 aluminum alloy and reported the effect of subsequent isothermal treatment parameters

Corresponding author: Ju-fu JIANG, Tel: +86-18746013176, E-mail: jiangjufu@hit.edu.cn;
Ying WANG, Tel: +86-15945697615, E-mail: wangying1002@hit.edu.cn
DOI: 10.1016/S1003-6326(24)66645-8
1003-6326/© 2024 The Nonferrous Metals Society of China. Published by Elsevier Ltd & Science Press
This is an open access article under the CC BY-NC-ND license (http://creativecommons.org/licenses/by-nc-nd/4.0/)

on the semisolid 7075 aluminum billets. BINESH and AGHAIE-KHAFRI [16] reported the acceleration effects on recrystallization and spheroidization of repetitive upsetting-extrusion (RUE) cycles in the RUE-based preparation of AA7075 aluminum alloy. CAO et al [17] quantitatively calculated the plastic energy stored in billet during radial strain and introduced rotary swaging (RS) into the process of the strain-induced melt activation (SIMA) to prepare semisolid C5191 alloy. All the above methods can successfully prepare semi-solid billets with excellent performance by solid state method, but there is a problem of long process and high cost. We have put forward wrought aluminum directly semisolid isothermal treatment process (WADSSIT) that is a method with a short process and low cost, and successfully applied this method to 2A12 alloy [18,19], 5A06 alloy [20,21] and 7075 alloy [22]. The key point of this method is that it can directly use the hot deformed wrought aluminum alloy that has been supplied in batches, which greatly shortens the process flow and reduces the cost. In addition, this idea of making billet also breaks the shackle that the solid phase of semi-solid billet must be fine and round to ensure formability. The research results on the preparation of 2A14 aluminum alloy billets by this method were published in previous research [23]. There is no report on the microstructure and mechanical properties of 2A14 aluminum alloy semi-solid forming parts for now.

The problem of engineering application of wrought aluminum alloy semi-solid processing technology not only lies in its complex billet preparation process and high billet cost, but also the lower mechanical properties of wrought aluminum alloy formed by semi-solid processing as compared with the forging state standard. In order to improve the mechanical properties of semi-solid parts, it is necessary to develop a deep understanding of the deformation mechanism of semi-solid metals. CHEN and TSAO [24] proposed four deformation mechanisms in the process of semi-solid metal deformation. It is worth noting that during the forming process of semi-solid metal, not only the liquid phase flows, but also some plastic deformation occurs in the solid phase, which provides an idea for deformation strengthening to improve the mechanical properties of semi-solid parts. CHEN et al [25] proposed a method of solid−liquid composite forming, and reported that the surface hardness of 7075 aluminum alloy increased due to deformation strengthening when the solid plastic deformation was enhanced. CHEN et al [26] reported the method of forming complex aluminum alloy by gradient temperature, and pointed out the effect of the solid deformation mechanism on deformation strengthening in the semi-solid forming process. In addition, in our forming experiments on 5A06 aluminum alloy, we also found that deformation strengthening can significantly improve comprehensive mechanical properties of 5A06 aluminum alloy in the thixo-forging process. The mechanical properties of the semi-solid thixoforged 5A06 aluminum alloy were better than those of the rolling state [21]. DEEPAK et al [27,28] reported the microstructure and tensile properties of the thixoformed A356−5TiB2 in-situ composite. The deformation strengthening effect caused by solid plastic deformation was caused by the specific microstructure of elliptical solid semi-solid billet during deformation. Ellipsoidal solid semi-solid billets were prepared by the WADSSIT method, which realized a combination of short process, low cost and high mechanical properties. At present, the applicability of this method to 2A14 aluminum alloy has not been verified.

Therefore, in order to verify the formability of this short flow method of preparation of 2A14 aluminum alloy semi-solid billet, and to study the mechanical properties and microstructure of 2A14 aluminum alloy, we thixoforged a complex box-shape part with a large wall-thickness difference of 2A14 aluminum alloy billets prepared by the WADSSIT method. The corresponding die and forming tooling were designed and manufactured based on a box-shaped part with complex shape and large wall-thickness difference. The feasibility of the process was verified, and the effect of forming parameters on the mechanical properties and microstructure was studied.

2 Experimental

2.1 Materials and preparation of semisolid billet

The material used in this work is 2A14 aluminum alloy hot-rolled plate purchased from Northeast Light Alloy Co., Ltd., of China, with a rolling cumulative deformation of 90%. The chemical composition of the aluminum alloy is

listed in Table 1. The main alloying element in the alloy is Cu, with a content of 4.370 wt.%, which is lower than the maximum Cu content that can be dissolved in solid high-temperature aluminum (5.65 wt.%). Due to deviating from the copper content of aluminum and copper binary eutectic alloy, the solid−liquid temperature range is very wide, but the casting performance is poor. Differential scanning calorimetry (DSC) result of 2A14 alloy was obtained via a STA449F3 differential scanning calorimeter. The semi-solid temperature range of the aluminum alloy is between 512 and 663 °C, and there is a pre-melted eutectic absorption peak between 512 and 530 °C. The heating rate during the test was 10 °C/min. These experimental results were published in our previous study [23].

In order to shorten the semisolid billet process, a novel method called wrought aluminum directly semisolid isothermal heat treatment (WADSSIT) based on strain-induced melting activated (SIMA) and recrystallization and partial melting (RAP) was used for the fabrication of semisolid billet. The commercial hot-rolled plate was cut into billets, directly continuously heated to semisolid temperatures and then held for 20 min. A box-type resistance furnace with PID control guaranteed temperature error within 1 °C was used for the isothermal treatment of billets.

2.2 Thixoforging process

Figure 1(a) shows the tooling used in thixoforging. And Fig. 1(b) shows the macrograph of the thixoforged 2A14 aluminum components at different temperatures. The whole tool consists of three parts, the upper die part, the lower die part and the ejector part. The whole tool is assembled on a 5000 kN universal hydraulic press. The semi-solid billet of 2A14 alloy was prepared by direct isothermal heat treatment of forged aluminum alloy. The billet was divided into cuboids of 194 mm × 50 mm × 77 mm, and the billet obtained by quantitative division was placed in a box-type electric resistance furnace for heating. The heating time was 1 h. Due to the anti-oxidation property of aluminum alloy, which can form a dense oxide film on the surface, the billet did not need vacuum protection, but was directly heated in the air atmosphere. The heating temperatures of the billet were 610, 620, 630 and 640 °C respectively, and the holding time was 20 min. The solid fraction of the 2A14 alloy at 610, 620, 630 and 640 °C were 0.82, 0.71, 0.59 and 0.45, respectively, as reported by our previous study [23]. We also conducted experiments with holding time of 5, 10 and 15 min. The results show that the formability of the billet was not good when the holding time was less than 15 min. Thixoforging part was a complex part with multiple deep cavities, thin walls and high ribs. Minimum wall thickness of 6 mm, maximum wall thickness of 25 mm, draft angle of only 1° and allowance of 1 mm leaving little oversize for machining achieved demonstrate the near-net shape of thixoforging. The part has the characteristics of large wall-thickness difference, and the maximum wall-thickness difference reaches 19 mm, which is also the difficulty of forming such complex parts by casting method. The female die was preheated to 400 °C, and the male die was preheated to 340 °C. The

Table 1 Chemical composition of hot rolled 2A14 aluminum alloy (wt.%)

Item	Cu	Si	Mn	Mg	Fe	Ti	Zn	Ni	Al
Experiment	4.370	0.916	0.781	0.589	0.177	0.025	0.027	0.006	Bal.
Standard	3.9−4.8	0.6−1.2	0.4−1.0	0.4−0.8	≤0.7	≤0.15	≤0.3	≤0.1	Bal.

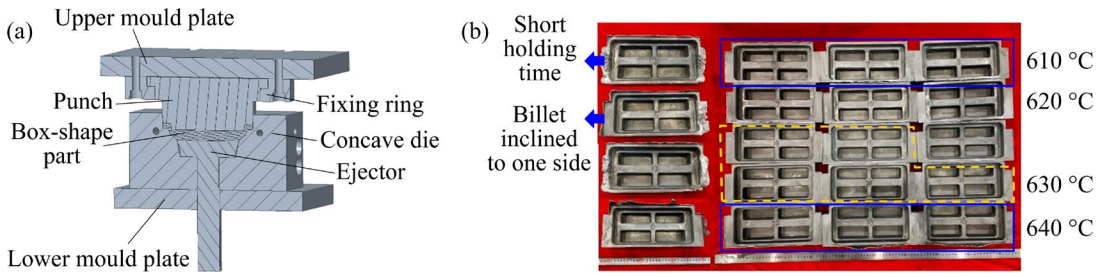

Fig. 1 (a) Thixoforging die design of box-shape part; (b) Macrograph of thixoforged 2A14 aluminum components at different temperatures

sectional area of the part was 35316 mm^2, and the equivalent static pressure under the pressure of 5000 kN hydraulic press was about 141 MPa. The dwell time was 45 s. Then, about 600 mL of room-temperature water was poured onto the part for online quenching, so that the part can establish sufficient strength for ejection. More detailed parameters have been disclosed in our authorized patent [29].

2.3 Analysis of microstructure and mechanical properties

Samples for the optical observation and mechanical properties test were cut from various positions of the thixoformed components. The samples were first ground with 200, 400, 800, 1500 and 2000 grit sandpapers, then mechanically polished on a gold velvet disc sprayed with 1 μm diamond powder at 2000 r/min for 5 min, and finally chemically etched with Keller's reagent. The chemical composition of the Keller's reagent was an aqueous solution with 2.5 vol.% HNO_3, 1.5 vol.% HCl, and 1 vol.% HF, and the etching time was 25 s. Optical microscopy (OM, Olympus GX71) was used for the capture of the microstructure image. The tensile specimens were cut into sheet dog bone with a gauge length of (32±0.05) mm, a thickness of (3±0.05) mm, a width of (6±0.05) mm, and a transition fillet of *R*6. The tensile properties were measured using the Instron 5569 testing machine and before that, the traces of electrical wire cut on the specimen were polished with 2000 grit paper. Three samples were taken from the tensile samples under each experimental parameter, the mechanical properties were taken as the average value, and the error bars were calculated to eliminate the influence of random error on the mechanical properties. The electron back scatter diffraction (EBSD) observation was conducted on a Zeiss Supra55 scanning electron microscope (SEM). Transmission electron microscope (TEM) was carried out on Talos F200X. The phases were determined by X-ray diffraction (XRD, Empyrean diffractometer) in the 2θ range of 20°−90° at a scanning speed of 10 (°)/min.

3 Results

3.1 Macrograph of thixoforged components

Figure 1(b) shows the macrograph of the thixoforged 2A14 aluminum components at different temperatures. In the forming process, due to the short holding time (shorter than 15 min), the parts could not be filled completely. When the holding time reaches 20 min, the parts can be filled completely. In addition, when the billet is placed into the die, improper operation causes the billet to be biased to one side of the die, which will also lead to half of the parts being filled, while the other half cannot be filled. It can be observed that the final filling part is the flange area on both sides of the part. With a short holding time, even if the pressure of the hydraulic press is high enough, the forming part will produce cold isolation in the flange area on both sides due to a less liquid phase, and the forming fails. When the holding time reaches 20 min, the parts can be fully formed. As shown in Fig. 1(b), the complete parts are successfully formed at the holding temperatures of 610, 620, 630 and 640 °C, respectively. The formed parts have clear contours, smooth appearance, high dimensional accuracy and a small flying edge, which successfully completes the near-net forming of the box-type parts.

3.2 Microstructure of thixoforged components

Figure 2 shows the microstructures of different regions in the formed parts. Figure 3 shows the average grain size of different regions in Fig. 2. Figure 2(b) shows the microstructure at the middle Position *A* of the part in Fig. 2(a). Most of the grains in the microstructure at Position *A* are relatively small in size, no larger grains are found, and relatively obvious plastic deformation forms are found, indicating that the deformation mechanism of this position is mainly the plastic deformation of solid phase during the forming process. Figure 2(c) shows the microstructure at Position *B* of the part in Fig. 2(a). Compared with Position *A*, Position *B* exhibits a duplex grain structure consisting of a small number of large sizes grains and a large number of small sizes grains. Although some large-sized grains were found in the microstructure in Location *B*, it also exhibits a plastic deformation characteristic. This illustrates that the deformation mechanism in Location *B* is not a solid−liquid phase mixing flow mechanism, but the plastic deformation mechanism of solid phase. Figure 2(d) shows the microstructure at flange Position *C* of the part in Fig. 2(a). The microstructure

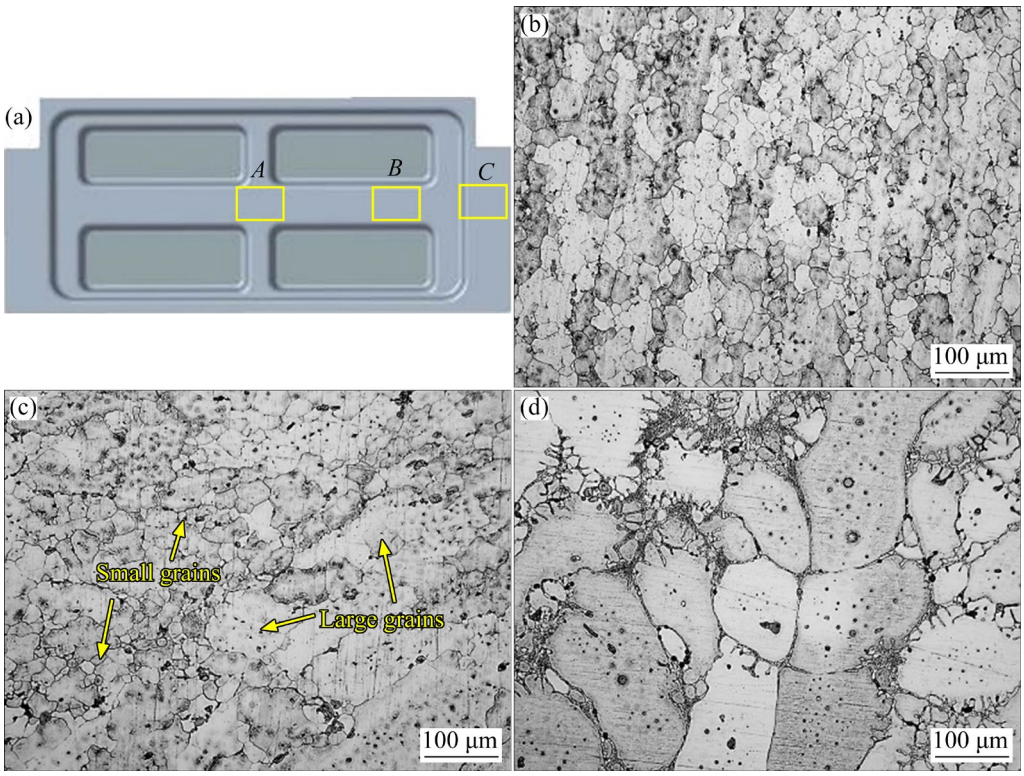

Fig. 2 Microstructures of different positions of thixoforged part: (a) Location diagram; (b) Position *A*; (c) Position *B*; (d) Position *C*

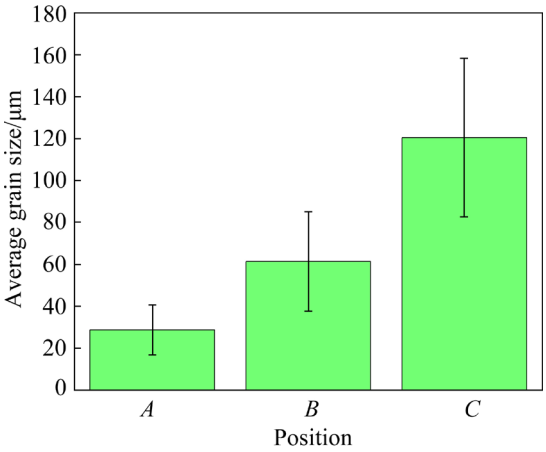

Fig. 3 Average grain size of different positions in thixoforged complex box-shape parts

at Position *C* is dominated by coarse grains, and an obvious solidification dendrite can be seen at the grain boundary, which indicates that the deformation mechanism of this position is dominated by solid−liquid phase mixed flow, and there is a certain liquid phase filling mechanism.

In order to further analyze the element distribution of the parts, the backscattered electron images at different positions and the element surface distribution were characterized by scanning electron microscopy. Figure 4 shows the SEM image at the middle Position *A* of the forming part. Figure 4(a) shows the image of backscattered electrons at the middle Position *A* of the forming part. The contrast diagram of backscattered electrons shows the light and dark by atomic number. It can be seen that the second phase at Position *A* is evenly distributed and isolated, and the size varies from several microns to tens of microns. Figures 4(b−g) show the surface distribution of Al, Cu, Mg, Si, Fe and Mn elements in the corresponding region, respectively. The distribution of Cu element in Fig. 4(c) coincides with most of the bright second phase in Fig. 4(a), indicating that most of the positions of the second phase contain Cu element. However, in a few second phase positions, there is no Cu element, and these regions are mainly enriched with Si, Fe and Mn elements. Figure 4(d) shows the distribution of Mg element. It can be seen that Mg element is completely uniformly distributed in the whole microstructure without any enrichment points, which indicates that Mg element exists in the solid solution. Figure 4(e) shows the surface distribution results of Si element. The distribution of Si element

and Cu element is close, but it does not completely coincide. Some rich points do not coincide with Cu. Figures 4(f, g) show the surface distribution of Fe and Mn elements, respectively. The distribution of enrichment points of Fe and Mn elements is relatively diffuse, and the two elements completely coincide. In addition, the enrichment points of Fe and Mn elements contain Si element. This indicates that Fe−Mn−Si phase exists in the microstructure. The grain at the middle Position *A* of the forming part is also relatively fine, and the second phase is distributed at the grain boundary. The element surface distribution diagram shows that Mg element mainly exists in the form of solute solution in the alloy, so the distribution is extremely uniform and there is almost no accumulation point. The elements Cu, Si, Fe and Mn are mainly metallic compounds.

Figure 5 shows the SEM image at flange Position *C* of the forming part. Figure 5(a) shows the backscattered electron image. Figures 5(b−g) show the surface distribution of Al, Cu, Mg, Si, Fe and Mn elements in the corresponding region, respectively. According to the backscattered electron image, the second phase at flange Position *C* is mostly distributed on the edge of the grain in a continuous shape, and its distribution shape is consistent with the eutectic structure of as-cast solidification, indicating that the liquid phase is the main solidified structure in the continuous distribution area of the second phase in the forming process. Comparing the distribution of Al and Cu elements in Figs. 5(b, c), it can be shown that the solid phase region is dominated by Al-rich matrix, while the liquid phase is dominated by Cu-rich eutectic structure. Interestingly, the distribution of Mg element shown in Fig. 5(d) is relatively uniform, and there is almost no obvious enrichment distribution, which indicates that the solid solution amount of Mg element in the solid phase is similar to that in the liquid phase. Figure 5(e) shows the

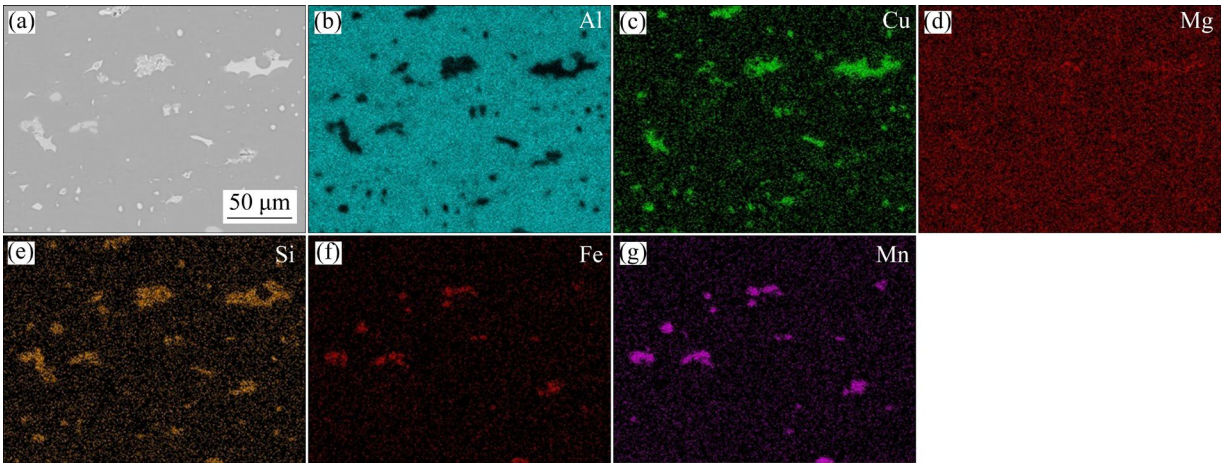

Fig. 4 SEM−EDS mapping images of 2A14 parts at middle Position *A*: (a) Backscattered electron image; (b) Al; (c) Cu; (d) Mg; (e) Si; (f) Fe; (g) Mn

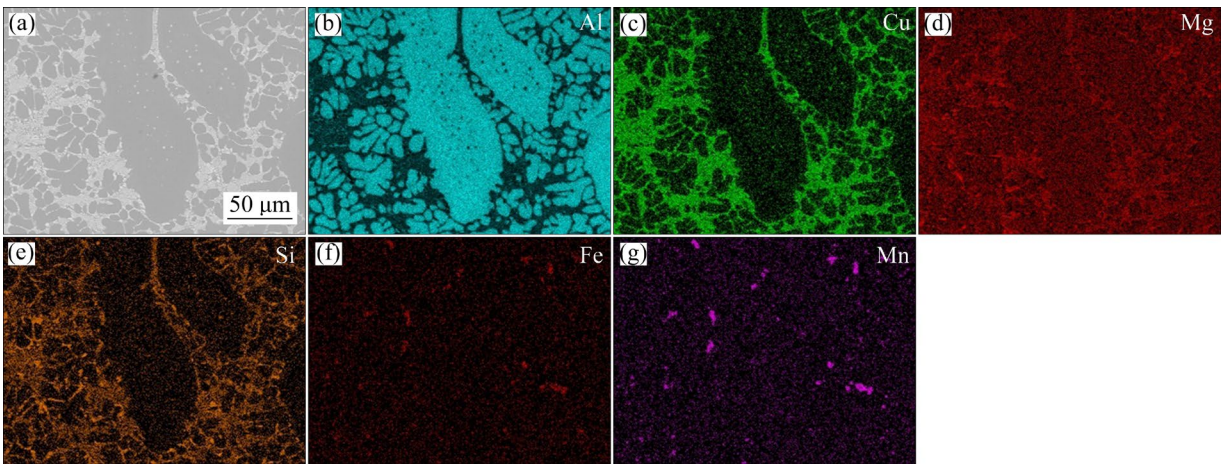

Fig. 5 SEM−EDS mapping images of 2A14 parts at flange Position *C*: (a) Backscattered electron image; (b) Al; (c) Cu; (d) Mg; (e) Si; (f) Fe; (g) Mn

distribution of Si element, whose grid-like distribution is almost the same as that of Cu element. Figures 5(f) and (g) are the surface distribution of Fe and Mn elements, respectively. Fe and Mn have similar enrichment points, but the distribution of the enrichment points is more uniform and isolated, which does not show the characteristics of continuous distribution like Cu and Si elements.

In order to more clearly characterize the distribution of the second phase in alloying elements, the microstructure was characterized by backscattered electron images at the higher magnification. The microstructure at flange Position *C* is selected here for illustration, because the content of the second phase at the flange position is higher, which can reflect the state of the second phase more clearly. Figure 6 shows the SEM-BSE images at the flange region under different magnifications. And Table 2 shows the corresponding EDS results of different regions in Fig. 6(b). As can be seen in Fig. 6(a), in the semi-solid microstructure, the liquid phase is mainly distributed at the grain boundary, but at the same time, a few liquid phases are distributed in the grains in the form of droplets. The distribution of the second phase is consistent with that of the liquid phase. The continuous distribution of the eutectic structure shows the network shape. As shown in Fig. 6(b), the network-like eutectic structure shows lamellar distribution, consisting of brighter θ-Al_2Cu (Region 2 in Fig. 6(b) and Table 2) and darker eutectic α(Al) (Region 1 in Fig. 6(b) and Table 2). In addition to the eutectic structure, an additional second phase was also observed (Region 3 in Fig. 6(b) and Table 2). According to the element surface distribution in Figs. 4 and 6, it can be inferred that the additional second phases are Fe, Mn and Si. Meanwhile, the second phase of regular hexagon can be observed in some areas, which is presumed to be monocrystalline silicon. According to the results in Fig. 6, in the region with more liquid phase, the second phase is mainly distributed in the alloy in a network connected by grain boundaries, and a few second phases are distributed in the matrix in a more diffuse and uniform form.

Figure 7 shows the XRD pattern of 2A14 alloy. The most dominant phase in the 2A14 alloy is α-Al matrix phase, followed by the θ-Al_2Cu phase. No other phases were evident in the composition of the 2A14 aluminum alloy. However, it can be seen from Figs. 4−6 that there were not only θ phase but also other phases in the alloy, and these phases could not be detected by XRD because their volume fraction was rarely lower than the threshold of XRD detection.

In order to determine the composition of the second phase more accurately and characterize the deformation state of the forming parts, the second phase was further characterized by transmission electron microscopy (TEM). The TEM sample was

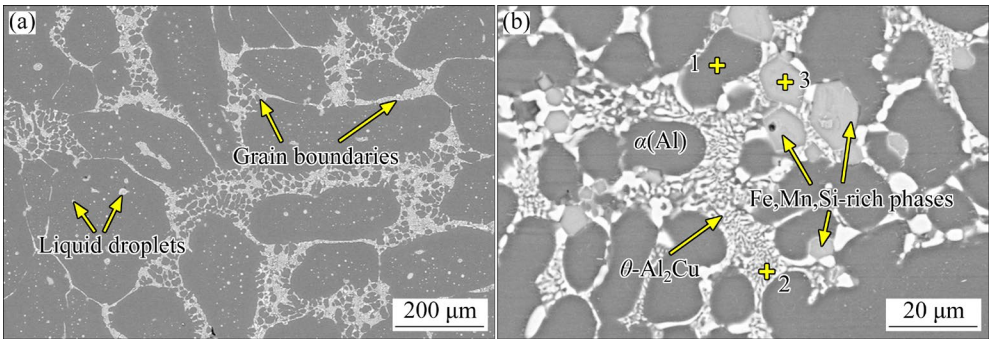

Fig. 6 SEM−BSE images of 2A14 parts at flange Position *C* under different magnifications

Table 2 EDS results of different regions in Fig. 6 (wt.%)

Region No.	Mg	Al	Si	Ti	Mn	Fe	Cu	Zn
1	0.25	97.56	0.70	0.18	0.02	−	1.09	0.20
2	1.89	57.90	3.54	0.05	1.95	0.40	34.27	−
3	−	61.29	6.58	0.01	18.63	10.41	3.05	0.03

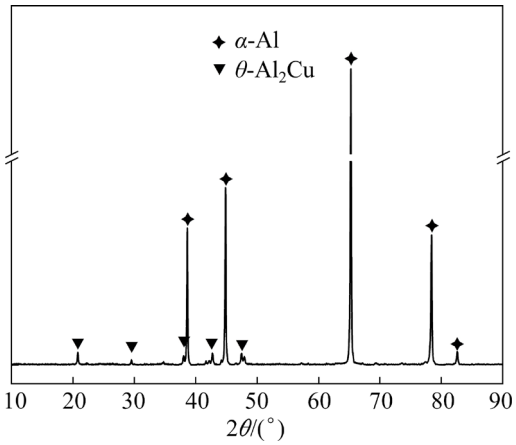

Fig. 7 XRD pattern of 2A14 aluminum alloy

taken from the middle Position *A* of the formed part. This is because the second phase content at flange Position *C* of the forming part is too much, and the second phase at flange Position *C* is mainly eutectic structure, so it is difficult to determine the second phase rich in Fe, Mn and Si. Meanwhile, the grain size at flange Position *C* is large. If the TEM sample is taken from flange Position *C* of the forming part, there will be fewer grains in the sampling area, and it is difficult to find Fe, Mn and Si phases in the thin area. In addition, in order to show the influence of plastic deformation in thixotropic forging, the plastic deformation of grains can also be observed under the bright field image by sampling from the central area *A* of the forming part.

Figure 8 shows the transmission electron micrograph of the 2A14 alloy parts, and Fig. 8(a) shows the high-angle annular dark field (HAADF) image. It can be observed that there are several second phases in the middle of the image with a size of several hundred nanometers. In Fig. 8, the large phase is FeMnSi phase, the copper-rich phase is θ-Al_2Cu phase, and the Zn element is solid dissolved in θ-Al_2Cu phase. The Mg_2Si phase is present. Figures 8(b−h) show the distribution of element energy spectra under scanning transmission electron microscope. It can be seen from Figs. 8(d, g, h) that FeMnSi phase is distributed in a hexagonal shape in the alloy. The Mg_2Si phase has a small size and is distributed in the alloy as a polygon.

The transmission electron micrograph in the 2A14 alloy parts is shown in Fig. 9. Figure 9(a) shows the HAADF diagram, and it can be observed that multiple second phases appear simultaneously in the diagram. The central phase is Mg_2Si phase. Surrounding the Mg_2Si phase is the (Mn, Fe)Al_6 phase. The disc on the left is the θ-Al_2Cu phase, and the Zn element is dissolved in the θ phase. This indicates that the second phases are usually precipitated at the same location.

In order to determine the composition of the second phase, the selected electron diffraction results are necessary in addition to the spectral analysis results. Figure 10 shows the select electron

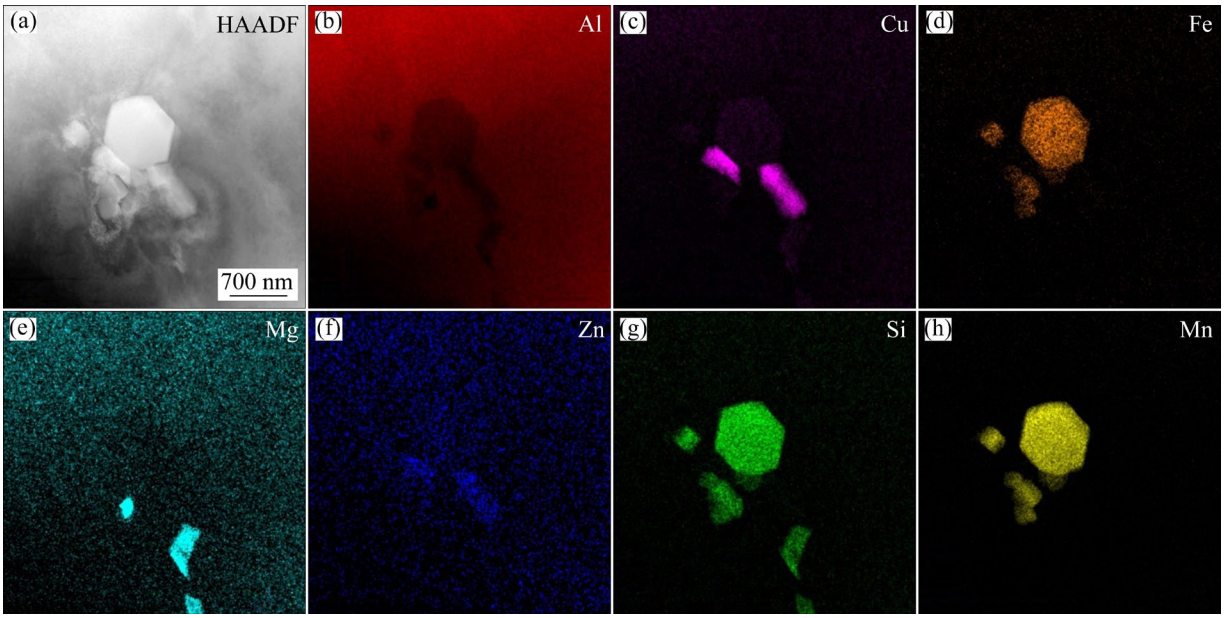

Fig. 8 STEM−EDS images of 2A14 part at middle Position *A*: (a) HAADF image of second phases; (b−h) EDS mapping images of main alloying elements of Al, Cu, Fe, Mg, Zn, Si and Mn, respectively

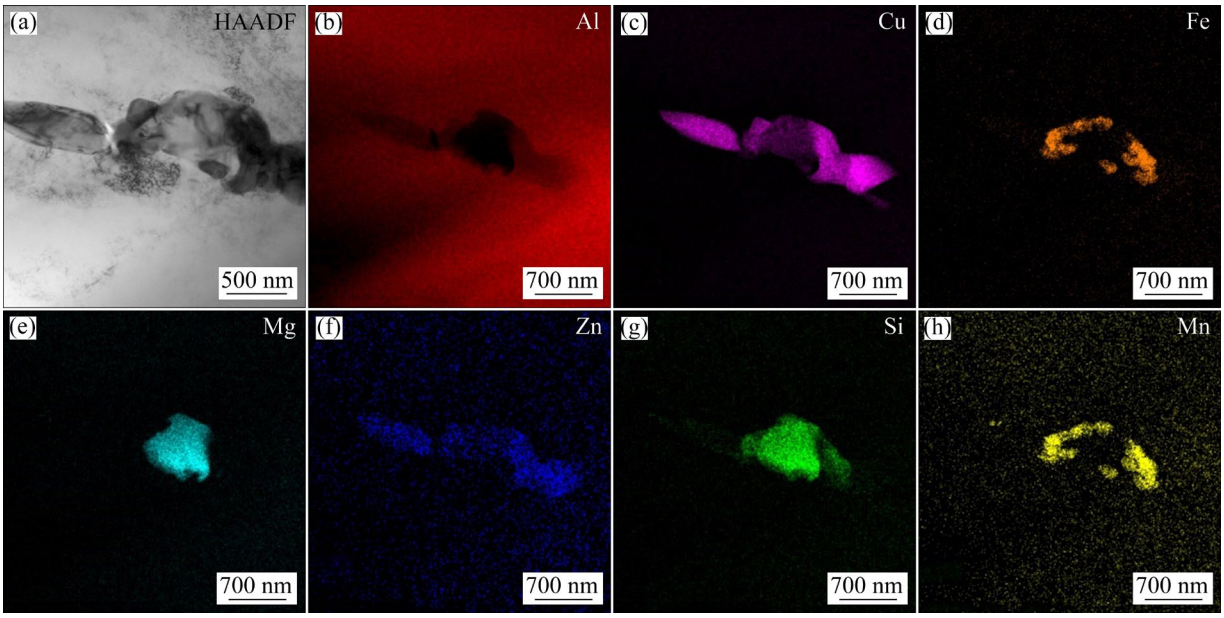

Fig. 9 STEM−EDS images of 2A14 part at middle Position *A*: (a) HAADF image of second phases; (b−h) EDS mapping images of main alloying elements of Al, Cu, Fe, Mg, Zn, Si and Mn, respectively

diffraction at the second phase position corresponding to Fig. 9 and its calibration results. Figures 10(a−c) show the bright field image, high-resolution image and the Fourier transform image at the position rich in Fe and Mn elements in Fig. 9, respectively. According to the PDF card calibration, the second phase in Fig. 9 was determined as $MnAl_6$ phase. In Fig. 9, an enrichment of Fe can be observed within the $MnAl_6$ phase. This occurs due to the solid solution of Fe elements in the $MnAl_6$ phase, resulting in the formation of the $(Mn,Fe)Al_6$ phase. Figures 10(d−f) show the bright field image, high-resolution image and selected electron diffraction images at the position rich in Mg and Si elements in Fig. 9, respectively. According to the PDF card calibration, it is inferred that the second phase is Mg_2Si phase. Figures 10(g−i) show the bright field image, high magnification image and selected electron diffraction images at the position rich in Cu and Zn elements in Fig. 9. According to the PDF card calibration the second phase is θ-Al_2Cu phase.

In order to illustrate the plastic deformation behavior of the alloy in the central deformation region, the results of the bright field image at a typical position under transmission scanning electron microscope are taken. Figure 11 shows the bright field image at the center Position *A* of the 2A14 alloy part. In the process of forming, the central Position *A* of the alloy is the first to contact with the mold, which gives priority to solidification (or liquid phase extrusion), so the alloy has undergone drastic plastic deformation, which can also be seen in Fig. 2(b). The morphology of the substructure can be observed more carefully under transmission electron microscope. Figure 11(a) shows the bright-field image of the FeMnSi phase and its surrounding matrix. FeMnSi phase plays a role in blocking dislocation movement during the deformation process of the alloy, resulting in a very obvious dislocation plug at the interface between the FeMnSi phase and the matrix, which plays a key role in the plastic deformation strengthening of the alloy. Figure 11(b) shows the interaction between Mg_2Si phase and dislocation. It can be obviously observed that Mg_2Si also plays a significant role in hindering the dislocation slip, which shows that the dislocation also forms a relatively obvious dislocation plug at the interface between Mg_2Si phase and matrix. Figure 11(c) shows the interaction between the more diffusely distributed FeMnSi phase and the dislocation. A relatively obvious dislocation bypass mechanism can be observed, which indicates that the diffusion-distributed FeMnSi phase also plays an obstacle role in the dislocation slip. Figure 11(d) shows the

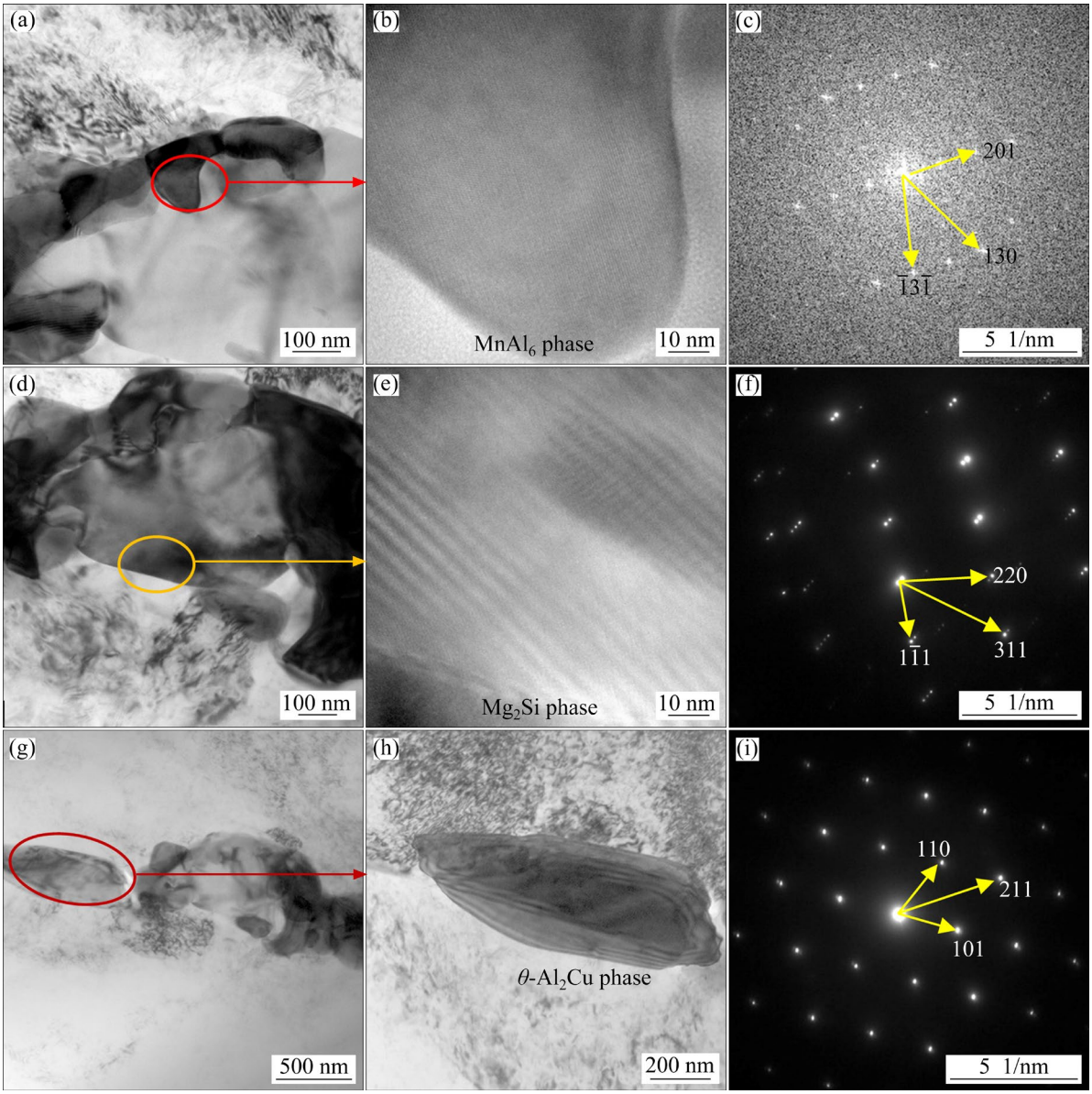

Fig. 10 TEM images of 2A14 part: (a, d, g) BF images of second phase; (b, e, h) High magnification images; (c, f, i) SAED patterns of corresponding images

high-density dislocation region created by the dislocation plug. Due to the existence of the high-density dislocation region, the further plastic deformation of the alloy is hindered and the deformation is strengthened. Figure 11(f) shows the dislocation wall substructure generated in the alloy, which indicates that the structure level of the alloy is further enriched under plastic deformation. Due to the high laminar fault energy of aluminum alloy, dislocation is more likely to cross slip and climb, so it is not easy to produce twin structures under severe plastic deformation, but tends to produce cellular structure. The creation of a dislocation wall means that the alloy grains break up.

3.3 Mechanical properties and fracture morphologies

Figure 12(a) shows the mechanical tensile curves of 2A14 aluminum alloy at different forming temperatures. It can be seen from the tensile curve that the fracture elongation is higher than 10% at the forming temperatures of 610−640 °C, which indicates that the forming property of the thixoforging part is good and there is no obvious defect in the forming part. The tensile strength of the forming parts increases first and then decreases with the increase in forming temperature. The mechanical properties of the forming parts reached a peak at 620 °C. At 610 °C, the proportion of solid

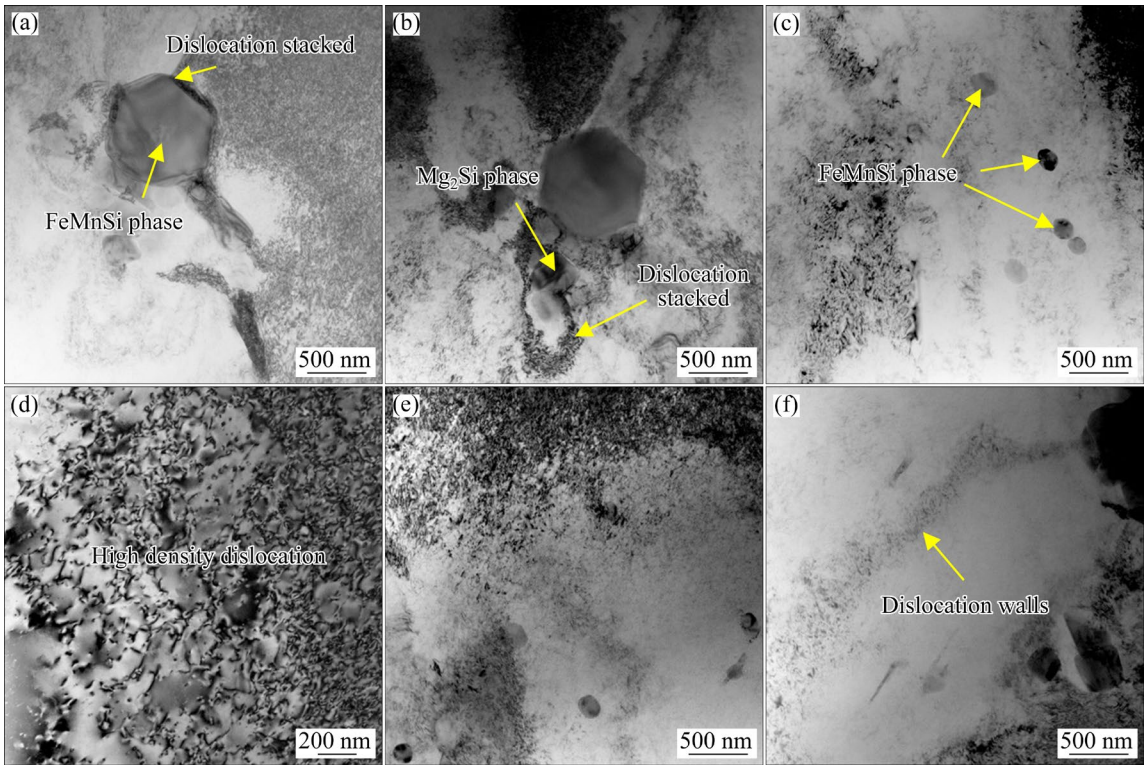

Fig. 11 Bright field images of 2A14 part at middle Position *A*: (a) FeMnSi phase; (b) Mg_2Si phase; (c) FeMnSi phase; (d, e) High-density dislocation; (f) Dislocation wall

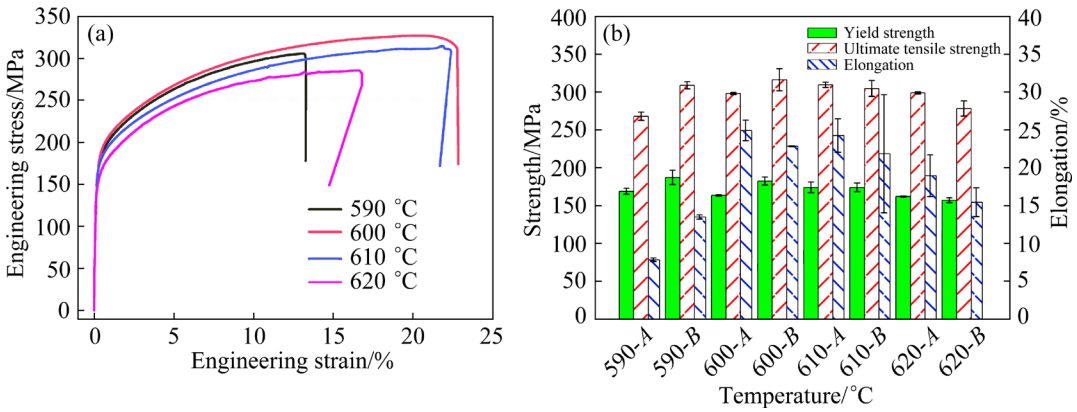

Fig. 12 Tensile curves at different forming temperatures (a), and mechanical properties at different forming temperatures and different positions (b) of directly thixoforged 2A14 parts

plastic deformation during thixotropic forging is the largest among several temperatures due to low temperature. Its theoretical deformation strengthening effect is expected to be optimal, evident from the higher yield strength and greater strain hardening rate observed on the tensile curve. Additionally, its fracture elongation rate is the lowest, indicating the highest consumption of plastic deformation capacity during the deformation process. However, its tensile strength is not the highest, or due to its large strain during deformation, the dynamic recrystallization state is related to the difference at 620−630 °C. With the increase in deformation temperature, the liquid fraction of the alloy increases gradually, and the strengthening effect of solid plastic deformation decreases gradually. When the deformation temperature is 640 °C, due to the high liquid fraction of the alloy, the solidification specific gravity increases, so that the micropores of the alloy are more than those of the parts under the low temperature forming condition, and the fracture elongation decreases. The yield strength (YS) and

ultimate tensile strength (UTS) were 176.5 and 322.2 MPa, and the elongation (EL) was 24.2%.

Figure 13 shows the morphology of tensile fracture of the forming parts at different forming temperatures. Figures 13(a−c) show the fracture morphology at a forming temperature of 610 °C. As shown in Fig. 13(a), at a lower magnification, the macro-morphology of the fracture shows a certain river pattern, indicating that the fracture is more brittle, which is consistent with the low fracture elongation of the 610 °C part in Fig. 13(b). Further enlarging the fracture morphology, it can be observed that there is a very small dimple morphology on the fracture, and a relatively obvious tearing edge structure can be observed, which indicates that the part has a certain fracture toughness. When the magnification is further increased, it can be seen that some of the second phase positions have very flat fracture morphology, while the Al matrix is dominated by dimple morphology. It shows that the fracture mechanism of the parts formed at 610 °C is a hybrid fracture form combining a ductile fracture and a brittle fracture. Figures 13(d−f) show the fracture morphology at 620 °C. It can be seen that obvious tearing structures can be observed in the fracture morphology at both lower and higher magnifications. Under the macroscopic fracture shown in Fig. 13(d), the upper left position of the fracture is the macroscopic tearing edge. As shown in Fig. 13(e), a significant number of small dimple structures are present at high multiples of the fracture surface. As shown in Fig. 13(f), extremely refined tear edges between the tiny dimples can be observed at higher magnification. This indicates that the fracture form of the parts formed at 620 °C is mainly ductile fracture, which is also consistent with the results in Fig. 12(b) that the parts formed at 620 °C have higher fracture elongation and better toughness. Figures 13(g−i) show the morphology of fracture at 640 °C. As shown in Fig. 13(g), an obvious river pattern can be observed at the macro

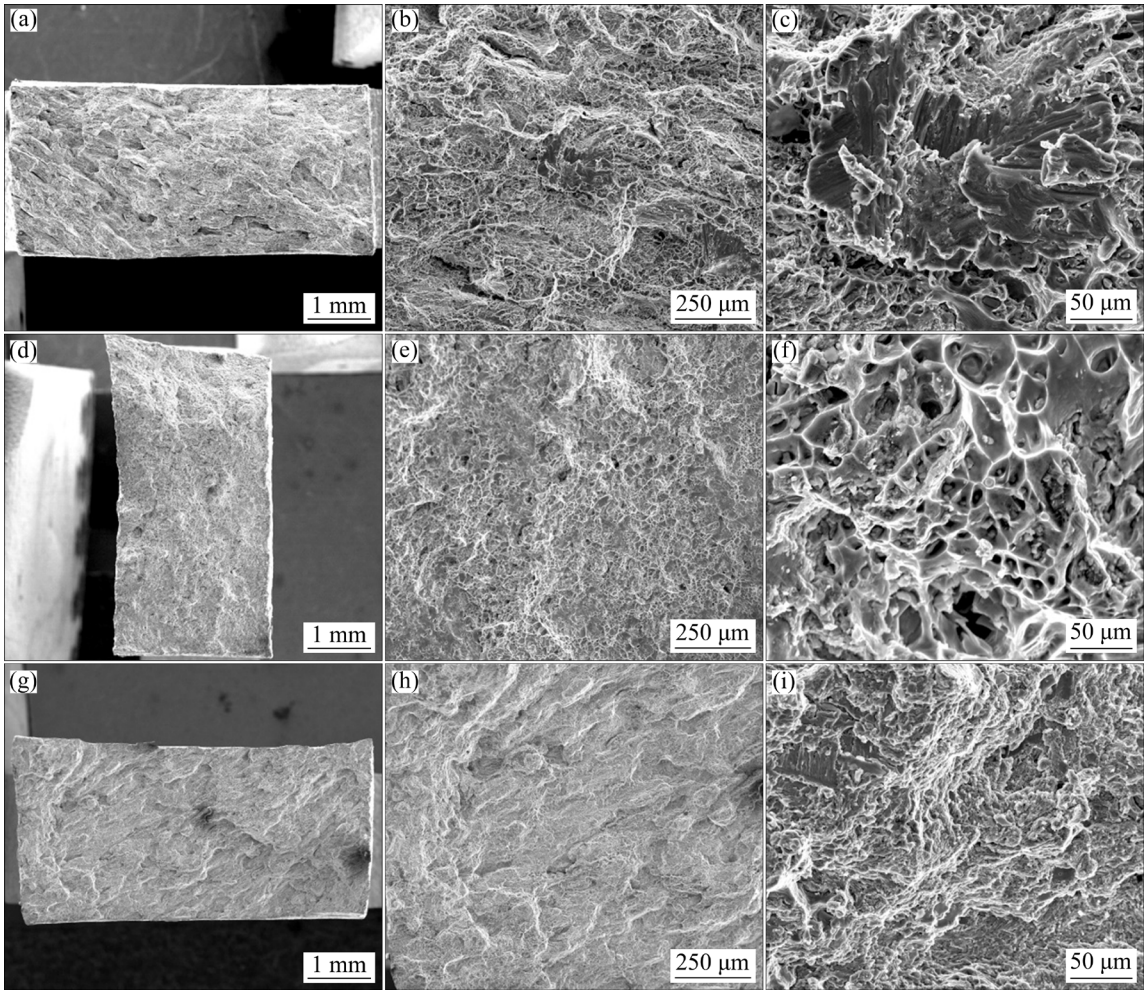

Fig. 13 Fracture surfaces of specimens thixoforged at different temperatures: (a−c) 610 °C; (d−f) 620 °C; (g−i) 640 °C

level, which indicates that this fracture has obvious brittle fracture characteristics. As shown in Fig. 13(h), obvious river patterns can also be observed in the fracture morphology at higher magnification, this can also explain why the fracture elongation of 640 °C parts was slightly lower than that of 620 °C parts, but its fracture elongation can still reach 15%, as shown in Fig. 12(b).

4 Discussion

4.1 Feasibility analysis

In fact, at the beginning of the study, different forming temperatures were set from 600 to 640 °C, and different holding time was set from 5 to 30 min (with a temperature rising time of 1 h). However, due to the poor forming performance of the parts under most experimental parameters, the mold was not fully filled to successfully form the complete parts. Therefore, this paper only selected parts whose holding temperature was 20 min to explore the influence of forming temperature on mechanical properties of forming parts. Thus, it can be seen that the application window of this process is relatively narrow. Many research studies have concentrated on the semi-solid formability of alloys, specifically targeting, the process window in order to forecast the semi-solid formability of various alloys. LIU et al [30] proposed a criteria for the prediction of thixoformability of aluminum alloy based on temperature sensitivity. Although the accuracy was not up to the mark, this method was widely used to predict the thixoformability of aluminum alloys because of its simplicity and directness. However, for pure metals or eutectic alloys, there was no solid−liquid temperature range, so the criterion based on temperature sensitivity fails. Under the temperature sensitivity criterion, there was no process window for metals without solid-liquid temperature range. This was contrary to the fact that the casting alloy with fixed melting points can be used for semi-solid processing. Thus, ZHANG et al [31] proposed a semi-solid process window criterion based on time sensitivity. This method can provide a good criterion for semi-solid formability of fixed melting point alloys. To further improve the accuracy of the criterion of alloy semi-solid formability, HU et al [32] proposed a novel criterion for assessing the semi-solid processing window of aluminum alloys based on the enthalpy sensitivity of liquid fraction. The prediction results of this method showed that the process window of 2014 aluminum alloy was slightly narrower than that of 7075 aluminum alloy, which was consistent with the results obtained in this work, that the semi-solid process window of 2A14 aluminum alloy was narrower. CHANG et al [33] reviewed the criteria for assessing the processability of semisolid alloys. The methods to judge the semi-solid formability of alloys based on temperature sensitivity, time sensitivity and enthalpy sensitivity are summarized, respectively, and it is believed that the enthalpy sensitivity based method is better consistent with the actual results, even though most studies are still more accustomed to judging the semi-solid formability of alloys based on temperature sensitivity. We did a similar experiment on the 2A12 alloy [19], and the results show that the process has better formability on the 2A12 alloy than on the 2A14 alloy. However, near-net forming of 2A14 alloy can still be successfully achieved by this process. This also shows that there is still a problem with the semi-solid formability criterion of aluminum alloy at present, that is, the difficulty of semi-solid formability can only be judged from a qualitative perspective, but the specific quantitative window range of semi-solid formability cannot be accurately given. In addition, the criteria for the formability of semi-solid alloys still remain in the study of the basic physical properties of the alloy, that is, the melting point, heating time, and the enthalpy of the alloy, and the effect of the semi-solid formability when the alloys had different semi-solid microstructure characteristics had not been discussed. Therefore, the judgment accuracy of the above criteria for the formability of semi-solid billets used in this study needs to be further studied.

4.2 Deformation mechanism and segregation of alloying elements

The semi-solid billets used in this study were prepared by the WADSSIT method [23]. This method has the characteristics of short process and low cost. At the same time, the solid phase of the semi-solid billets prepared was elongated ellipsoid, which was different from the formability of conventional semi-solid billets with equiaxed near spherical solid phase. Based on the phenomenalism

and solid-phase coherence theory [34], it can be judged that the critical coherent solid fraction of semi-solid billets with ellipsoidal solid phase will be lower than that of equiaxed solid phase, which means that the fluidity of ellipsoidal semi-solid billets is inferior to that of equiaxed solid semi-solid billets. This difference magnified the difference between solid and liquid phase fluidity on the parts formed in this study. As proposed by CHEN and TSAO [24], four deformation mechanisms are to be the major mechanisms controlling the deformation of alloys with non-dendritic microstructure in semi-solid state, they are the liquid flow (LF) mechanism, the flow of liquid incorporating solid particles (FLS) mechanism, the sliding between solid particles (SS) mechanism, and the plastic deformation of solid particles (PDS) mechanism. In this work, due to the difference of filling sequence, it is considered that the PDS mechanism was dominant in the middle of the box-shaped part and the FLS and SS mechanisms were dominant in the flange area.

In addition, because the enrichment of alloy elements would reduce the melting point of the alloy, the content of alloy elements in the eutectic composition of the liquid phase was significantly higher than that of the solid phase, resulting in significant macro element segregation in Figs. 2−7. The distribution of Cu element in the middle of the part is obviously lower than that in the flange of the part. It is worth noting that the segregation of the alloy element was not shown on Fe, Mn and Si elements, but only on Cu element, which also shows that other alloy elements were mostly in the state of solid solution in the matrix during the forming process, while Cu element was mainly in the state of melting into liquid phase. This has not been reported on the previous semi-solid forming parts, which is due to the ellipsoidal shape of the solid phase microstructure of the semi-solid billet used in this study. The formation reason and compression deformation behavior of semi-solid ellipsoidal solid were reported in our previous research [23,35]. This macro element segregation phenomenon is something we do not want to see. Since the forming state of the formed part is not the final service state, and the heat treatment process is also required, we hope that the segregation of this alloy element can be improved after heat treatment. LAN et al [2] investigated the influence of heat treatment parameters on the strengthening effect of 2A14 alloy. The artificial aging process of 2A14 aluminum alloy was optimized by JMA equation calculation and XRD aided test. HUANG et al [1] proposed non-isothermal aging (NIA) treatment method to improve the comprehensive mechanical properties and intergranular corrosion (IGC) resistance of 2A14 aluminum alloy. This solution and artificial aging or improved solution and artificial aging process were considered to be the most effective heat treatment process to improve the service properties of 2A14 alloy. At present, there is no research on the improvement of the heat treatment process of semi-solid forming parts. Our research results show that the distribution of alloy elements in semi-solid forming parts was obviously different from that in traditional forming processes, so the heat treatment process of semi-solid forming parts should be improved. In particular, in order to realize the long-term migration of alloy elements, the solution process should extend the solution time compared with the solid solution of solid plastic forming parts.

4.3 Mechanical properties

The mechanical properties of the formed parts belong to the unique characteristics of the formed state, not the final service state, but the study of the influence of the forming process parameters on the mechanical properties of the formed parts can help deeply understand the semi-solid deformation behavior. JIANG et al [21] successfully formed a complex 5A06 aluminum alloy bracket by direct semi-solid thixoforging. The effect of solid plastic deformation on deformation strengthening in semi-solid forming was emphasized. This method is consistent with the thixoforging method used in this work, and the conclusion also supports the experimental results. Figure 12(b) shows the mechanical properties of thixoforged parts at different forming temperatures, the yield strength of the formed parts gradually increased with the decrease in temperature, which indicates that the reduction of temperature was helpful to improving the deformation strengthening effect of solid plastic deformation. CHEN et al [26] investigated the microstructure of 7075 alloy parts formed by a solid−liquid compound forming with a temperature gradient, and they found that the formed parts obtained a microstructure gradient similar to the

temperature gradient. With the increase of the controlled temperature gradient during the forming process, the microstructure of the formed part changes gradually from the pure solid plastic deformation microstructure to the semi-solid filling deformation microstructure. This is similar to the idea of deformation strengthening by reducing semi-solid forming temperature to achieve solid plastic deformation. Although the mechanical properties in the forming state still need heat treatment, which was not the final service performance, the highest performance strengthening could often be obtained after heat treatment under the forming process parameters with the highest mechanical properties and excellent morphology. JIANG et al [19] studied the influence of the heat treatment process on the mechanical properties of semi-solid forming 2A12 aluminum alloy, and found that the mechanical properties of the formed parts under the optimal forming process parameters, can still be maintained the highest after T6 heat treatment.

The main strengthening mechanisms of the thixoforging 2A14 parts were considered as solution strengthening, deformation strengthening and second phase strengthening. The solute atoms in α-Al matrix cause lattice distortion, which obstructs the movement of dislocations, making the slip process difficult to execute, and the solid-solution strengthening effect is more obvious. In addition, the semi-solid 2A14 alloy experienced obvious plastic deformation during thixoforging. On the one hand, plastic deformation would introduce a large number of dislocations in the matrix, and the increase in dislocation density in the matrix will hinder further slip and climb of dislocations, which also means that the high stress is required to make the parts deformed. On the other hand, plastic deformation will introduce substructure into the matrix, refine and segment large grains to produce fine grains. The yield strength of the formed parts will also be improved according to the classical Hall−Petch formula [36]:

$$\sigma^*=\sigma_0+Kd^2 \quad (1)$$

where σ^* is the yield strength; σ_0 is the friction force to prevent dislocation slip; K is the influence coefficient of orientation difference of adjacent grains on the dislocation movement, which is commonly known as grain boundary resistance, and its magnitude is related to the crystal structure; d is the grain diameter.

5 Conclusions

(1) The box-shaped component with complex shape and a large wall-thickness difference was successfully formed. The filling sequence of semisolid slurry during the thixoforging of the box shape component involves filling of the middle, filling of the side wall and filling of the flange. There is obvious solid−liquid segregation behavior in the whole part, which is mainly caused by the extrusion of liquid phase during deformation. This is followed by the segregation of the eutectic structure at the flange position. However, the dispersion distribution of FeMnSi phase did not show obvious macroscopic segregation. Large deformation was noted in the microstructure of the thixoforged parts. It is beneficial to improving the mechanical properties of the thixoforged parts.

(2) The yield strength varied from 157.1 to 187.3 MPa, the ultimate tensile strength varied from 268.2 to 316.6 MPa, and the elongation varied from 7.8% to 24.9%. The optimum process parameter of direct thixoforging 2A14 aluminum alloy was held at 620 °C for 20 min.

(3) In the thixoforging process, there are obvious solid plastic deformation characteristics in the center of the first formed parts, and deformation strengthening is more obvious. The flange position of the post-formed part is dominated by the solid−liquid mixed filling deformation mechanism, and there is an obvious solidification dendrite structure at the grain boundary of large grains. The non-uniform macro distribution of the liquid phase also causes the macro segregation of Cu element on the parts.

CRediT authorship contribution statement

Ying-ze LIU: Methodology, Software, Formal analysis, Investigation, Data curation, Writing − Original draft preparation, Visualization; **Ju-fu JIANG:** Conceptualization, Resources, Supervision, Project administration, Funding acquisition; **Ying ZHANG**, **Min-jie HUANG** and **Jian DONG:** Validation, Writing − Review and editing; **Ying WANG:** Conceptualization.

Declaration of competing interest

The authors declare that they have no known

competing financial interests or personal relationships that could have appeared to influence the work reported in this paper.

Acknowledgments

This work is supported by the National Key R&D Program of China (No. 2022YFB3404204), the National Natural Science Foundation of China (No. U2241232), and the Foundation of National Key Laboratory for Precision Hot Processing of Metals, China (No. 6142909230203).

References

[1] HUANG Lan-ping, HE Long-long, CHEN Song-yi, CHEN Kang-hua, LI Ji-yu, LI Song, LIU Wen-sheng. Effects of non-isothermal aging on microstructure, mechanical properties and corrosion resistance of 2A14 aluminum alloy [J]. Journal of Alloys and Compounds, 2020, 842: 155542.

[2] LAN Jian, SHEN Xue-jun, LIU Juan, HUA Lin. Strengthening mechanisms of 2A14 aluminum alloy with cold deformation prior to artificial aging [J]. Materials Science and Engineering A, 2019, 745: 517−535.

[3] SHI Chen, WU Yong-jun, MAO Da-heng, FAN Gao-feng. Effect of ultrasonic bending vibration introduced by the L-shaped ultrasonic rod on solidification structure and segregation of large 2A14 ingots [J]. Materials, 2020, 13(3): E807.

[4] YU Wen-fang, ZHAN Li-hua, XU Yong-qian, CHEN Kai, YANG You-liang, XU Ling-zhi, PENG Nan-hui, MA Bo-lin, LIU Cong, CHEN Zan-chong. Temperature-dependent creep aging behavior of 2A14 aluminum alloy [J]. Journal of Materials Research and Technology, 2022, 19: 1343−1354.

[5] WANG Bing-xiang, YI You-ping, HE Hai-lin, HUANG Shi-quan. Effects of deformation temperature on second-phase particles and mechanical properties of multidirectionally-forged 2A14 aluminum alloy [J]. Journal of Alloys and Compounds, 2021, 871: 159459.

[6] ZHOU Bing, LU Shuai, XU Kai-le, XU Chun, WANG Zhan-yong, WANG Bin-jun. Hot cracking tendency test and simulation of 7075 semi-solid aluminium alloy [J]. Transactions of Nonferrous Metals Society of China, 2020, 30(2): 318−332.

[7] LI Gan, QU Wen-ying, LUO Min, CHENG Le, GUO Chuan, LI Xing-gang, XU Zhen, HU Xiao-gang, LI Da-quan, LU Hong-xing, ZHU Qiang. Semi-solid processing of aluminum and magnesium alloys: Status, opportunity, and challenge in China [J]. Transactions of Nonferrous Metals Society of China, 2021, 31(11): 3255−3280.

[8] LIN Bo, FAN Tao, LI Hao-yu, ZHAO Yu-liang, ZHANG Wei-wen, LIU Kun. Microstructure and high temperature tensile properties of Al−Si−Cu−Mn−Fe alloys prepared by semi-solid thixoforming [J]. Transactions of Nonferrous Metals Society of China, 2021, 31(8): 2232−2249.

[9] YANG Xiang-jie, YU An-shan, ZHENG Bin, GUO Hong-min. Microstructure evolution of a semisolid magnesium alloy slurry obtained via an internal rapid cooling stirring process (IRCSP) [J]. Metallurgical and Materials Transactions B, 2020, 51(6): 2895−2904.

[10] EFTEKHAR A H, SADROSSADAT S M, REIHANIAN M. Statistical optimization of electromagnetic stirring parameters for semisolid AM60 slurry using Taguchi-based grey relational analysis [J]. International Journal of Metalcasting, 2022, 16(1): 212−222.

[11] VICARIO I, CRESPO I, VAL D, WEISS U, CAO D, MARTINEZ I, SANCHEZ J M. Development of a squeeze semisolid high-pressure die casting process for magnesium structural parts [J]. Journal of Materials Engineering and Performance, 2019, 28(7): 3935−3940.

[12] MORADJOY-HAMEDANI M, ZAREI-HANZAKI A, FATEMI S M. Characterization of semisolid deformation behavior of a high Zr-containing WE magnesium alloy [J]. Rare Metals, 2022, 41(12): 4201−4208.

[13] SHAKIRIN M A, ABD RAZAK N A, AHMAD A H. A short review on grain refinement techniques in semisolid metal processing [C]//International Conference on Mechanical Engineering Research. Singapore: Springer, 2023: 909−918.

[14] CZERWINSKI F. Thermomechanical processing of metal feedstock for semisolid forming: A review [J]. Metallurgical and Materials Transactions B, 2018, 49(6): 3220−3257.

[15] MESHKABADI R, FARAJI G, JAVDANI A, POUYAFAR V. Combined effects of ECAP and subsequent heating parameters on semi-solid microstructure of 7075 aluminum alloy [J]. Transactions of Nonferrous Metals Society of China, 2016, 26(12): 3091−3101.

[16] BINESH B, AGHAIE-KHAFRI M. RUE-based semi-solid processing: Microstructure evolution and effective parameters [J]. Materials & Design, 2016, 95: 268−286.

[17] CAO Miao, ZHANG Qi, ZHANG Yi-sheng. Effects of plastic energy on thixotropic microstructure of C5191 alloys during SIMA process [J]. Journal of Alloys and Compounds, 2017, 721: 220−228.

[18] JIANG Ju-fu, ZHANG Ying, WANG Ying, XIAO Guan-fei, LIU Ying-ze, ZENG Li. Spheroidizing process of 2A12 aluminum alloy grains during heating up and semisolid isothermal treatment stages [J]. Journal of Materials Engineering and Performance, 2021, 30(8): 5974−5986.

[19] JIANG Ju-fu, ZHANG Ying, WANG Ying, XIAO Guan-fei, LIU Ying-ze, ZENG Li. Microstructure and mechanical properties of thixoforged complex box-type component of 2A12 aluminum alloy [J]. Materials & Design, 2020, 193: Article 108859.

[20] JIANG Ju-fu, LIU Ying-ze, XIAO Guan-fei, WANG Ying, XIAO Xin-quan. Effects of temperature and time on microstructural evolution of semisolid 5A06 aluminum alloy: Preparation of semisolid billets in ellipsoid solid phase [J]. Journal of Materials Engineering and Performance, 2020, 29(8): 5346−5359.

[21] JIANG Ju-fu, LIU Ying-ze, XIAO Guan-fei, WANG Ying, XIAO Xin-quan. Effects of plastic deformation of solid phase on mechanical properties and microstructure of wrought 5A06 aluminum alloy in directly semisolid thixoforging [J]. Journal of Alloys and Compounds, 2020, 831: Article 154748.

[22] XIAO Guan-fei, JIANG Ju-fu, LIU Ying-ze, WANG Ying,

GUO Bao-yong. Recrystallization and microstructure evolution of hot extruded 7075 aluminum alloy during semi-solid isothermal treatment [J]. Materials Characterization, 2019, 156: Article 109874.

[23] LIU Ying-ze, JIANG Ju-fu, XIAO Guan-fei, ZHANG Ying, HUANG Min-jie, WANG Ying. Effects of temperature and time on three-dimensional microstructural evolution of semi-solid 2A14 aluminum alloy during short process preparation of semi-solid billets [J]. Transactions of Nonferrous Metals Society of China, 2022, 32(7): 2091−2109.

[24] CHEN C P, TSAO C Y A. Semi-solid deformation of non-dendritic structures—I. Phenomenological behavior [J]. Acta Materialia, 1997, 45(5): 1955−1968.

[25] CHEN Gang, CHEN Qiang, QIN Jin, DU Zhi-ming. Effect of compound loading on microstructures and mechanical properties of 7075 aluminum alloy after severe thixoformation [J]. Journal of Materials Processing Technology, 2016, 229: 467−474.

[26] CHEN Qiang, CHEN Gang, JI Xing-hua, HAN Fei, ZHAO Zu-de, WAN Jia, XIAO Xin-quan. Compound forming of 7075 aluminum alloy based on functional integration of plastic deformation and thixoformation [J]. Journal of Materials Processing Technology, 2017, 246: 167−175.

[27] DEEPAK KUMAR S, MANDAL A, CHAKRABORTY M. On the age hardening behavior of thixoformed A356−5TiB_2 in-situ composite [J]. Materials Science and Engineering A, 2015, 636: 254−262.

[28] DEEPAK KUMAR S, MANDAL A, CHAKRABORTY M. Effect of thixoforming on the microstructure and tensile properties of A356 alloy and A356-5TiB2 in-situ composite [J]. Transactions of the Indian Institute of Metals, 2015, 68(2): 123−130.

[29] JIANG Ju-fu, LIU Ying-ze, WANG Ying, XIAO Guan-fei, ZHANG Ying, HUANG Min-jie. Semi-solid thixotropic forging device for aluminum alloy thin-walled high-reinforced deep cavity casing portions, has middle cavity whose center is machined with square through hole into which two-section square rod is passed: China Patent, ZL202011119782.2 [P]. 2023−02−07.

[30] LIU D, ATKINSON H V, JONES H. Thermodynamic prediction of thixoformability in alloys based on the Al−Si−Cu and Al−Si−Cu−Mg systems [J]. Acta Materialia, 2005, 53(14): 3807−3819.

[31] ZHANG Du-yao, DONG Hong-biao, ATKINSON H V. What is the process window for semi-solid processing? [J]. Metallurgical and Materials Transactions A, 2016, 47(1): 1−5.

[32] HU X, HU Z, QU W, LI X, LI Z, ZHOU Y, MIDSON S P, ZHU Q. A novel criterion for assessing the processability of semi-solid alloys: The enthalpy sensitivity of liquid fraction [J]. Materialia, 2019, 8: 100422.

[33] CHANG Zhi-yu, WANG Xing-chen, WU Yu-juan, PENG Li-ming, DING Wen-jiang. Review on criteria for assessing the processability of semisolid alloys [J]. Materials Letters, 2021, 282: 128835.

[34] GOURLAY C M, DAHLE A K. Dilatant shear bands in solidifying metals [J]. Nature, 2007, 445(7123): 70−73.

[35] LIU Ying-ze, JIANG Ju-fu, ZHANG Ying, HUANG Min-jie, WANG Ying. Semi-solid compression of 2A14 alloy with high solid fraction: rheology, constitutive equation and microstructure [J]. Journal of Materials Science, 2022, 57(34): 16507−16527.

[36] LI Shi-ju, WEI Bo-wen, XU Jiu-jian, XU Guang-ming, LI Yong, WANG Zhao-dong. High solid-solution strengthening mechanism of a novel aluminum-lithium alloy fabricated by electromagnetic near-net shape technology [J]. Materials Science and Engineering A, 2022, 829: 142148.

直接触变锻造大壁厚差复杂壳体 2A14 合金件的显微组织与力学性能

刘英泽[1]，姜巨福[1]，张 颖[1]，黄敏杰[1]，董 健[1]，王 迎[2]

1. 哈尔滨工业大学 材料科学与工程学院 金属精密热加工国家级重点实验室，哈尔滨 150001；
2. 哈尔滨工业大学 机电工程学院，哈尔滨 150001

摘 要：针对大壁厚差复杂壳体件的成形，提出一种低成本、短流程的 2A14 合金直接触变锻造工艺，并进行验证。结果表明，复杂零件可以成功进行触变锻造。触变锻件组织中的固相晶粒表现出较大的变形程度，这使得触变锻件的力学性能有明显的改善。在显微组织中没有发现明显的液相偏析。触变锻造的 2A14 合金零件具有较高的力学性能，其屈服强度为 157.1~187.3 MPa，极限抗拉强度为 268.2~316.6 MPa，伸长率为 7.8%~24.9%。较大的晶粒尺寸和较小的晶粒圆整度使塑性变形程度增大，有利于提高触变锻件的力学性能。

关键词：触变锻造；显微组织；力学性能；2A14 铝合金

(Edited by Xiang-qun LI)